Thickness Dependent Ordering in Laterally Confined Monolayers of Spherical-Domain Block Copolymers

Gila E. Stein,[†] Won Bo Lee,[†] Glenn H. Fredrickson,[†] Edward J. Kramer,*[,†,‡] Xuefa Li,[§] and Jin Wang[§]

Department of Chemical Engineering, University of California, Santa Barbara, California 93106, Department of Materials, University of California, Santa Barbara, California 93106, and Advanced Photon Source, Argonne National Laboratory, Argonne, Illinois 60439

Received November 6, 2006; Revised Manuscript Received April 23, 2007

ABSTRACT: Monolayers of spherical-domain block copolymer, exhibiting hexagonal symmetry with a (10) periodicity of 25 nm, are laterally confined in hexagonal wells 12 μm wide and 26 nm deep that span the entire area of a two-inch diameter silicon wafer. The structure is characterized with grazing-incidence small-angle X-ray diffraction, which provides a quantitative measure of the positional and orientational order over macroscopic areas. Results are interpreted within the KTNHY framework for 2D phase behavior. At $T = 210$ °C, films that are 41 nm thick (monolayer plus brush) form oriented single crystals where the close-packed rows of the lattice are aligned with the edges of the wells. Translational order is determined to decay algebraically with a correlation function of the form $g_T(r) \sim r^{-0.25}$, consistent with a KTNHY 2D crystal having a shear modulus $\mu = 1.7 \times 10^{-4}$ N/m. Orientational order is long-range, with a full width at half-maximum of 1.1°. Decreasing the film thickness by 1 nm results in hexatic ordering with a translational correlation length on the order of 0.5 μm, and diminished orientational order with a full width at half-maximum of 2.4°. Scanning force microscopy measurements of the thickness-dependent defect structure are consistent with the crystalline and hexatic phase behavior measured by diffraction.

Introduction

Thin films of block copolymers are an ideal system for patterning on nanometer length scales, since they self-assemble into ordered phases where the domain size, periodicity, and morphology can be tuned by adjusting molecular weight and copolymer composition.[1] However, in the absence of an external field, these systems form randomly oriented grains in the plane of the film. This is unacceptable for applications that require precise placement of domains, such as high-density storage media,[2] and has inspired many efforts to better control ordering, grain orientation, and registration to features on or in the substrate. Techniques like the application of electric fields,[3,4] epitaxy on commensurate chemical patterns,[5−7] shearing,[8,9] and topographic patterning[10−12] (graphoepitaxy) are all effective in inducing alignment. This latter technique is particularly attractive for applications in the semiconductor industry, where topographic features can be produced with established lithographic methods, registered relative to features on the substrate, and readily integrated into existing manufacturing practices. The effects of substrate topography on block copolymer order has been the focus of much research, with demonstrated improvements in domain positioning and registry.[13−16]

It is well-established that long-wavelength phonons destroy translational periodicity in two-dimensional (2D) crystals,[17] which is arguably the leading impediment to obtaining precise domain positioning. The most widely accepted description of 2D phase behavior is the KTNHY theory, which predicts that a 2D crystal will have long-range orientational order, but algebraically decaying translational order.[18−21] At higher temperatures, the 2D crystal melts via a hexatic intermediate to the 2D liquid. Translational order is short-range in both the hexatic and liquid, but the hexatic possesses some 6-fold symmetry. Attempts to verify this behavior in block copolymers have utilized direct measurement of the lattice by scanning force microscopy to calculate correlation functions. In one case, behavior consistent with the KTNHY 2D crystal was reported, with long-range orientational order and approximately algebraic decay of translational order measured from a 2 μm^2 area.[22] A separate study reported good orientational order over a 6 μm^2 region, but short-range translational order, behavior consistent with a quenched hexatic phase.[23] However, the accuracy of quantitative measurements by scanning force microscopy is questionable due to thermal drift distortions, and the small sampling areas result in poor statistics.

Grazing-incidence small-angle X-ray diffraction (GISAXD) was recently used to characterize single crystals of spherical-domain block copolymer monolayers.[24] Analysis of the diffraction line shape within the context of the KTNHY theory demonstrated the long-range orientational order and algebraically decaying translational order characteristic of a 2D crystal. The clear advantage of diffraction over microscopy is statistics: A single GISAXD measurement covers areas on the order of 3 mm^2, roughly 10^6 times the area sampled by a single high-resolution scanning force microscopy image. However, details regarding the defect structure and defect density can only be inferred indirectly from such diffraction experiments.

In this paper, grazing-incidence small-angle X-ray diffraction is utilized to demonstrate an effect of monolayer thickness on translational and orientational order, and results are interpreted within the KTNHY framework. The diffraction experiments are complemented by scanning force microscopy measurements to characterize the thickness-dependent defect structure. A monolayer of spherical-domain block copolymer, exhibiting hexagonal

* To whom correspondence should be addressed. E-mail: edkramer@mrl.ucsb.edu.
[†] Department of Chemical Engineering, University of California, Santa Barbara.
[‡] Department of Materials, University of California, Santa Barbara.
[§] Advanced Photon Source, Argonne National Laboratory.

10.1021/ma062559a CCC: $37.00
Published on Web 07/14/2007

symmetry with a lattice parameter of 29 nm, is laterally confined in 12 μm wide hexagonal wells. When the film thickness (monolayer plus brush) is $t_f = 41$ nm, slow cooling from the order−disorder transition produces single crystals spanning the area of the 12 μm wide wells. The close-packed rows align parallel to the edges, which is the expected conformation to minimize elastic deformation,[10] so the crystal orientations across the entire substrate are correlated. The measured phase behavior is consistent with that of a 2D crystal having a shear modulus $\mu = 1.7 \times 10^{-4}$ N/m, and a translational correlation function with the form $g_T(r) \sim r^{-0.25}$. Decreasing the film thickness to $t_f = 40$ nm disorders the lattice, producing a hexatic phase with a correlation length on the order of 0.5 μm.

Diffraction Line Shape Analysis. Within the KTNHY framework for 2D crystalline phases, the translational correlation function decays algebraically as $g_T(\mathbf{r}) \sim r^{-\eta_G}$, and the delta-function Bragg peaks characteristic of long-range translational order are replaced by power law singularities of the form $S(\mathbf{q}) \sim |\mathbf{q} - \mathbf{G}|^{-2+\eta_G}$, where $\mathbf{q}$ is the in-plane scattering vector and $\mathbf{G}$ is a reciprocal lattice vector.[19] To quantify translational order, the parameter of interest is the KTNHY decay exponent

$$\eta_G = k_B T|\mathbf{G}|^2 c/4\pi\mu \quad (1)$$

where $c = (3 + \lambda/\mu)/(2 + \lambda/\mu)$, the parameters $\mu(T)$ and $\lambda(T)$ are the Lamé elastic constants (μ is the shear modulus). At the transition from crystalline to hexatic, the finite limiting values for λ and μ result in the bounds $^1/_4 < \eta_{10} < {}^1/_3$. In practice, power law singularities in the structure factor are not observed. Most real systems contain finite-sized crystallites that broaden the peak shape, which is well described by the analytic form of the 2D structure factor derived by Dutta and Sinha,[25]

$$S(\mathbf{q}) = S_0\{{}_1F_1(1 - \eta_G/2; 1; -|\mathbf{q} - \mathbf{G}|^2L^2/4\pi)\} \quad (2)$$

${}_1F_1$ (a;b;c) is the Kummer confluent hypergeometric function,[26] the parameter L is the crystallite size, and S_0 is a constant prefactor. The maximum crystallite size that can be measured is determined by the experimental resolution.

Hexatic phases are characterized by exponentially decaying translational order of the form $g_T(\mathbf{r}) \sim e^{-r/\xi}$, with a finite correlation length $\xi(T)$. The hexatic structure factor is well described by a Lorentzian function,[27]

$$S(q) = S_0\kappa^2/[\kappa^2 + |q\text{-}G|^2] \quad (3)$$

with $\kappa = 1/\xi$, except very close to the transition from the hexatic to the isotropic liquid, where a square-root Lorentzian may be more appropriate.

Orientational order for all phases is quantified by fitting the azimuthal $I(\Phi)$ data to the Fourier series,[28]

$$I(\Phi) = I_0\left(\frac{1}{2} + \sum_{n=1}^{\infty} C_{6n}\cos(6n\Phi)\right) \quad (4)$$

where the harmonic amplitudes C_{6n} are orientational order parameters, the first diffraction peak is centered at $\Phi = 0$, and I_0 is a constant prefactor. When the coefficients all approach unity, the series represents the Fourier transform of a δ-function, describing a crystal with perfect orientational order.

Experimental Methods

Lithography. An approximately 26 nm thick layer of silicon oxide was electron beam evaporated onto a 2 in. diameter silicon wafer. An array of 12 μm wide hexagonal wells separated by 2 μm wide mesas, spanning the entire area of the silicon wafer, was defined by the following photolithography process: The wafers were rinsed in deionized water to remove dust particles from the oxide surface, followed by a 10 min dehydration bake at 120 °C. The oxide surface was primed by exposure to hexamethyldisilazane (HMDS) vapors at room temperature for 10 min. Clariant AZ P4110 photoresist was spun cast at 4000RPM for 1 min, producing a 1 μm thick film, which was followed by a soft bake at 95 °C for 1 min. Samples were exposed to a broadband UV lamp at an intensity of 7.5 mW/cm^2 for 9.5 s in hard contact mode using a Karl Suss MJB 3 UV 400 mask aligner, then developed in pre-diluted (1:4 by volume) Clariant AZ 400K developer for 30−45 s. A 20 s descum step was performed immediately prior to etching. A Panasonic inductively coupled plasma etch system, operating with 0.3 Pa CHF_3 plasma, was used to produce the 26 nm deep hexagonal wells. The resulting radius of curvature in the corners of the hexagonal wells is approximately 1 μm, and the sidewall angle (controlled by the etch pressure) is no more than 20° off normal (see Figure 1, parts a and b). Unexposed resist and etch residue were removed by soaking in Rohm and Haas PRX 127 stripper at 80 °C for 1 h, then the wafers were cleaned in piranha solution (H_2SO_4:30 wt % H_2O_2, 3:1 vol/vol) to destroy any residual organic contamination. Piranha solution is highly oxidizing, and produces a 2 nm thick oxide layer covering the etched surfaces (the bottoms of the wells). Precautions undertaken when handling Piranha included wearing a full face shield, acid resistant apron, and heavy duty rubber gloves.

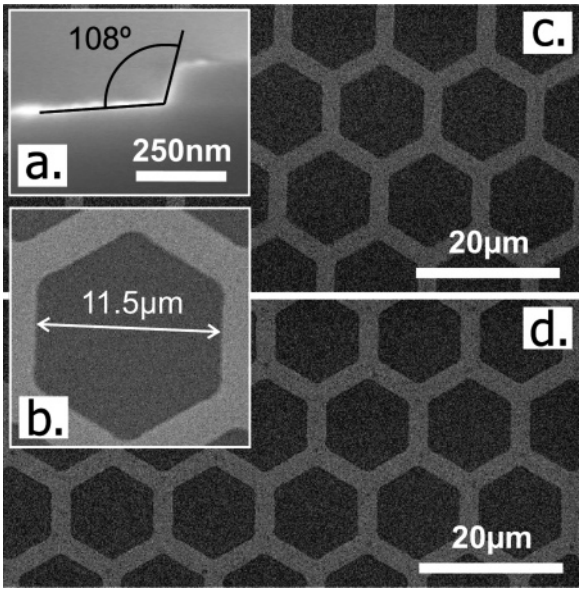

Figure 1. SEM measurements: (a) Sidewall angle produced by a 0.3 Pa CHF_3 etch, measured from a 100 nm deep oxide well. (b) Enlarged view of a hexagonal well. Bright regions correspond to the oxide mesas. (c, d) Grating with a 41 nm (c) and 40 nm (d) thick film in the wells and an approximately 18 nm thick brush on the mesas, demonstrating uniform coverage of the grating.

Polymer Synthesis. Poly(styrene-*b*-2vinylpyridine) (PS−PVP) was synthesized by anionic polymerization, producing a polydispersity index of 1.04, an overall degree of polymerization $N = 626$, and a composition of 12% PVP by volume. The PVP minority block forms spherical domains in a PS matrix. In 2D, the spheres arrange in a hexagonal lattice with a lattice parameter of approximately 29 nm at 210 °C.

Sample Preparation. All sample preparation was completed in a class 100 clean room. A PS−PVP film of thickness t_i was spun cast from a 1 wt % toluene solution onto the patterned substrates. PVP strongly wets the substrate, producing a brush layer approximately 18 nm thick covering the entire surface. The equilibrium thickness of a layer of spheres is approximately 23 nm at 210 °C, so if $t_i = 41$ nm, a complete layer of spheres covering both the mesas and wells will result. However, the objective is to

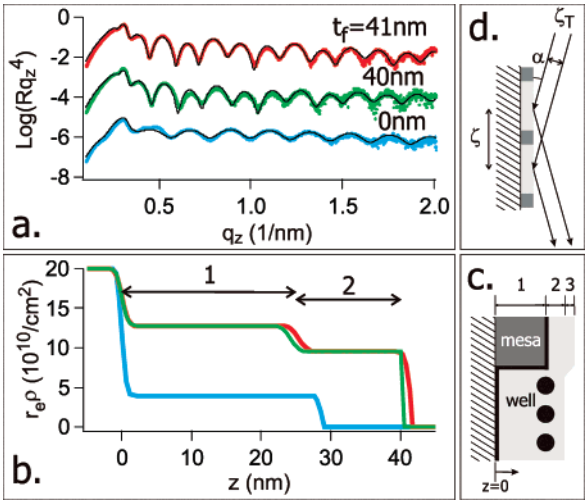

Figure 2. (a) Reflectivity data fit to the Parratt formalism. The thickness of the film in the well (monolayer plus brush) was calculated for each sample. The curve labeled $t_f = 0$ nm is an empty hexagon. (b) Electron density variation through the depth of the film. (c) Schematic of the sample cross-section (not to scale). The PVP domains/brush are colored black. (d) Schematic to show how the coherence length ζ depends on the incident angle α and the spatial coherence of the X-ray source ζ_T.

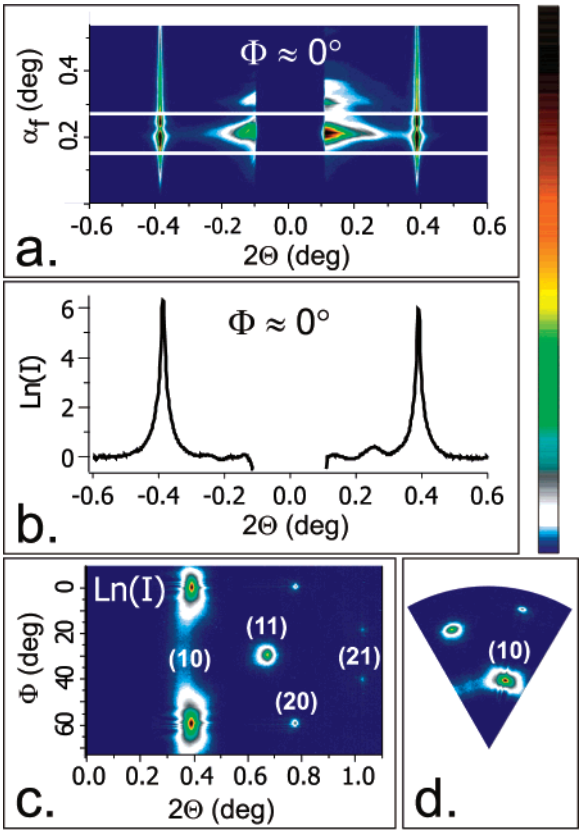

Figure 3. (a) Example of diffraction data collected at $\Phi \approx 0$. The scattering at low $q/2\Theta$ is from the hexagonal wells. (b) Background corrected line profile for $\Phi \approx 0$. Data is integrated over the bounds marked in part a. (c) Compiled $I(2\Theta, \Phi)$ data, in arbitrary units, constructed from line profiles like that shown in part b. Scattering data from the microstructure are symmetric about the beam stop at $2\Theta = 0$. The small peak at $2\Theta = 0.25$ is scattering from the edges of the hexagonal wells, which is strongly dependent on Φ and asymmetric unless the edges are perfectly parallel to the incident beam. (d) 60° segment from part c, shown in a radial plot. Plotting this 60° segment with 6-fold symmetry produces the "powder" maps shown in Figure 6.

produce a monolayer of spheres only in the wells. This results when the initial film thickness is $t_i \approx 33-35$ nm, so during annealing almost all the spheres on the mesas are drawn into the wells to produce the monolayer.[29] Samples were annealed under high vacuum (10^{-7} Torr) by first heating at 260 ± 6 °C for 6 h, which is above the 2D order−disorder transition (ODT) of 232 ± 5 °C, then cooling at a rate 0.03 °C/min to 210 ± 3 °C, and annealing isothermally 1.5 days. Temperature was actively monitored during annealing by a thermocouple connected to a small copper block located next to the sample. Upon removal from the oven, samples were rapidly quenched below the glass transition of PS−PVP (100 °C) to freeze the structure. Cooling from the ODT consistently produces single crystals in each well,[30] provided the film thickness is optimal. (The optimum film thickness is temperature dependent.) In contrast, a short heating period from room temperature to 210 ± 5 °C followed by a 3 days isothermal anneal results in low angle grain boundaries. This is illustrated by the scanning force microscopy images in Figure 4.

For analysis of the domain ordering by scanning force microscopy, an etch step to the midplane of the PVP spheres is necessary. Samples were etched with secondary ion mass spectrometry using the O_2^+ beam at a voltage of 1 kV, current of 25 nA, and a raster size of 0.15 mm^2. Charge compensation was provided by a static 600V electron beam. Negative ions of C^-, CN^-, and Si^- were monitored as a function of time (depth), where the CN^- signal is unique to PVP. The SIMS etch was stopped just after the first maximum in the CN^- signal, indicating the location of the midplane of the spheres. The PVP etches slightly faster than the PS matrix, resulting in a 1 nm height difference between the PVP core and the surrounding PS matrix. The exposed PVP cores also show phase contrast in SFM measurements, because PVP has a stronger adhesive interaction with the tip.

X-ray Reflectivity. The total thickness t_f of the PS−PVP film in the wells (monolayer of spheres plus brush) was measured by X-ray reflectivity using a Philips X'Pert MRD operating at a wavelength of 0.154 nm (Cu Kα). Fit results and the corresponding electron density profiles normal to the substrate are shown in Figure 2, parts a and b. A schematic of the sample cross-section (side view) is shown in Figure 2c. The reflectivity for each sample was fit by nonlinear regression to the Parratt recursions[31,32] convolved with a Gaussian resolution function having a half-width at half-maximum 10^{-2} cos(α) nm^{-1}, where α is the incident angle. The following are adjustable parameters: The layer thicknesses d_1, d_2, and d_3, the roughness of each interface, the sample length (which specifies the beam footprint as a function of incident angle),[33] and the fraction of the sample area occupied by the mesas x_M (which fixes the average lateral density for layers 1 and 3).

The thickness of the film in the wells is $t_f = d_1 + d_2$. We find $t_f = 41.1 \pm 0.1$ nm and $\chi^2 = 13$ for the top profile (red), while $t_f = 40.1 \pm 0.1$ nm and $\chi^2 = 30$ for the middle profile (green). The regression analysis is insensitive to the scattering from layer 3, and always converges to $d_3 = 0$ nm regardless of the initial guess. However, from scanning force microscopy measurements we know that $d_3 \sim 2$ nm. Therefore, we cannot accurately measure the brush thickness $t_b = d_2 + d_3$, and we are unable to calculate the monolayer thickness $t_M = t_f - t_b$. Note that errors in d_3 do not impact t_f: For example, if d_3 is constrained to 5 nm, $t_f = 41.2 \pm 0.1$ nm and 40.1 ± 0.1 nm for the top and bottom data sets, respectively.

Also shown in Figure 2, parts a and b are data for an "empty" hexagon (in blue, labeled $t_f = 0$). The thickness of the oxide mesa is 29 nm, and $\chi^2 = 7$. These data demonstrate that the coherence length at the sample surface $\zeta = \zeta_T/\sin\alpha$ is larger than the periodicity of the wells, even at high angles of incidence (see illustration in Figure 2d).[34,35] The spatial coherence of the source $\zeta_T \simeq \lambda R/r_S$ is approximately 1.2 μm, where the source to sample distance is $R = 320$ mm, and the source extension is $r_S = 0.04$ mm. This results in a coherence length $\zeta = 50$ μm at $\alpha = 1.4°/q_z = 2$ nm^{-1}, which is more than 3 times the periodicity of the hexagons.

Grazing-Incidence Small-Angle X-ray Diffraction (GISAXD). GISAXD experiments were conducted on the Sector 8-ID-E

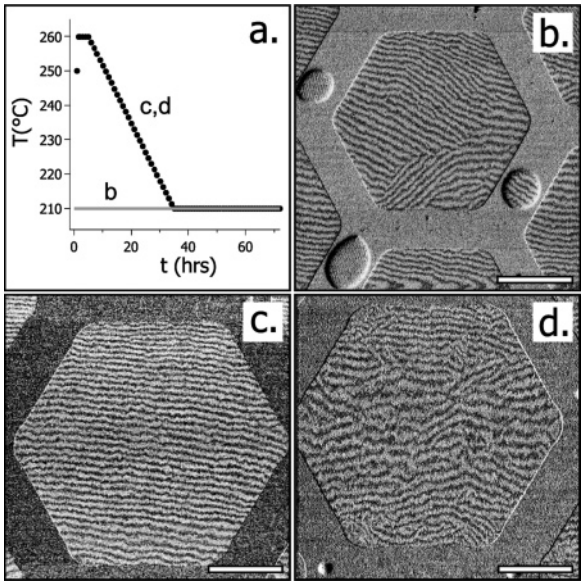

Figure 4. Moiré interference patterns in scanning force microscopy phase images. These are used to characterize the effect of thermal history on the resulting order, following the annealing schedules shown in part a. (b) $t_f \approx 41$ nm. Short heating period followed by a 3 day isothermal anneal at 210 °C. Low angle misalignments are observed in the moiré fringes, corresponding with underlying low-angle grain boundaries in the lattice. Islands of excess material are observed on the mesas. (c) $t_f = 41$ nm. Cooling from ODT at a rate 0.03°/min, followed by an isothermal anneal at 210 °C for 1.5 days, results in a single grain spanning the area of a 12 μm wide well. (d) $t_f = 40$ nm. Dislocations and misalignments in the lattice are observed when the film is 1 nm thinner than optimal. Scale bar = 3.5 μm.

beamline at the Argonne National Laboratory Advanced Photon Source, with an X-ray energy of 7.45 keV (0.164 nm). The sample to detector distance was 2256 mm, determined by calibration with a silver behenate standard ($d = 58.376$ Å). For all measurements, the incident angle was fixed at 0.195°, which is above the critical angle of the polymer, and below that of the silicon substrate. A lead beam stop blocked the strong specular reflections. The off-specular diffracted intensity was recorded with a 2D detector having a resolution of 79 μm/pixel, and data were stored as 2048 × 2048 tiff images. Each data set is a map of intensity $I(2\Theta, \alpha_f)$, where 2Θ and α_f denote the in-plane and out-of-plane diffraction angles. In the small angle approximation, the in-plane scattering vector is $q = 4\pi\Theta/\lambda$.

To measure the orientation of the crystals, samples were rotated in-plane over a range of at least 85°. Both the rotation increment $\Delta\Phi$ and exposure times varied for each sample, from $\Delta\Phi = 0.2°$ and 5 s exposure times for the best-ordered crystals, to $\Delta\Phi = 0.25°$ and 15 s exposures for the ones with hexatic-like order. Maps of intensity $I(2\Theta, \Phi)$ are constructed from the series of measurements as follows: A profile of intensity $I(2\Theta)$ is extracted from each $I(2\Theta, \alpha_f)$ data set by averaging in the range $0.17° < \alpha_f < 0.3°$, where the diffracted intensity is a maximum due to X-ray standing waves inside the film, and then background corrected by fitting a polynomial baseline. Each profile $I(2\Theta)$ corresponding with an angle Φ is used to build the array $I(2\Theta, \Phi)$. Intensities scales are normalized to correct for exposure times. The data in this paper are displayed in 6-fold symmetric polar surface plots to resemble conventional powder diffraction patterns, where the radius is 2Θ (or q) and the azimuthal angle is Φ. This data compilation process is illustrated by Figure 3.

For radial (q) line shape analysis, the samples were oriented in-plane such that $I(\Phi)$ was a maximum, which occurs when the edges of the hexagonal wells are parallel to the incoming beam. This orientation is denoted $\Phi = 0°$. The low-q scattering from the edges of the hexagons is extremely distinctive and was used as an alignment reference (see Figure 3a). Data were collected for 2 s at $\Phi = 0°$ to measure the (10) reflection. A secondary beam stop was inserted to block the strong (10) reflection, and the (20) reflection was measured by collecting data for 60 s. Samples were then rotated to $\Phi = 30°$ to measure the (11) reflection, and data were collected for 30 s. Ten areas were measured for each step to improve statistics, and the data were summed to provide a signal well above the background level.

The shape of the direct beam (the resolution function for line shape analysis) was measured by removing the principal beam stop and heavily attenuating the beam to prevent detector saturation. Data were collected for a total of 5 s. The profile was fit to the sum of two Gaussian functions centered at $q = 0$ and the area normalized to unity, resulting in the resolution function $R(q) = 312e^{-341789q^2} + 3.5e^{-12774q^2}$, where q is in units of nm^{-1}. The maximum crystal size that can be detected is between 1 and 2 μm, and is principally limited by the detector pixel size.

The sample height was aligned and the incident angle calibrated prior to every measurement (automatically by a macro statement). The beam intensity was recorded with a pin diode detector in front of the beam stop, and the sample height was set to the position where the intensity is reduced to half the maximum. The incident angle was calibrated with $\alpha - 2\alpha$ scans in the specular plane. These steps are particularly crucial for the rotation experiments, where we observe offsets in the incident angle up to 0.03° with a 0.2° change in Φ, which shifts the position and intensity of the maxima in $(2\Theta, \alpha_f)$ space.

Scanning Force Microscopy (SFM). All measurements were taken with a Veeco Metrology Group Digital Instruments Dimension 3000 SFM. High resolution measurements of the lattice were obtained using 1.25 × 1.25 μm^2 scan areas, while moiré interference patterns were generated with 13.5 × 13.5 μm^2 scan areas. All data were stored at a resolution of 512 × 512 pixels per image. The theory behind moiré patterns was presented elsewhere,[36,37] but we briefly recap the aspects that are relevant to this paper: The moiré fringes result from interference between the close-packed rows of the block copolymer lattice with the SFM scan lines. The periodicity and orientation of the fringes correspond with that of the underlying lattice, so multiple interference patterns per measurement indicates that the block copolymer sample has a polygrain structure. Furthermore, defects that disrupt the translational periodicity (such as isolated dislocations) appear in the moiré patterns as the termination or insertion of an extra fringe. For all measurements shown in this paper, the hexagon was aligned with an edge parallel to the fast scan axis. If the block copolymer lattice is aligned with the close-packed rows parallel to the edge, which is the expected conformation to minimize elastic deformation, the moiré fringes will also be parallel to the edge of the well.

Scanning Electron Microscopy (SEM). All measurements were taken with an FEI XL40 Sirion FEG microscope operating at an acceleration voltage of 5 kV. The sidewall image was collected in ultrahigh-resolution mode at a working distance of 5 mm and 50K times magnification.

Results and Discussion

Thermal History and Monolayer Thickness. The results presented in this paper were obtained by first heating the monolayer to 260 ± 6 °C to disorder the lattice, then cooling at a rate 0.03 °C/min to 210 ± 3 °C, and annealing isothermally for 1.5 days. Cooling from the order−disorder transition always produces single crystals in the 12 μm wide wells,[30] provided the film thickness is optimal. In contrast, heating from room-temperature directly to 210 °C results in low-angle grain boundaries, even in wells that are only 9 μm wide. These effects of thermal history and monolayer thickness are demonstrated by the SFM phase images in Figure 4a-d, where moiré interference patterns permit the grain structure across the entire well to be characterized with a single measurement. We believe that as the monolayer is cooled from the liquid through the hexatic phase, the grain orientation forms at the edges of the wells and propagates to the center.[38] The resulting single grain

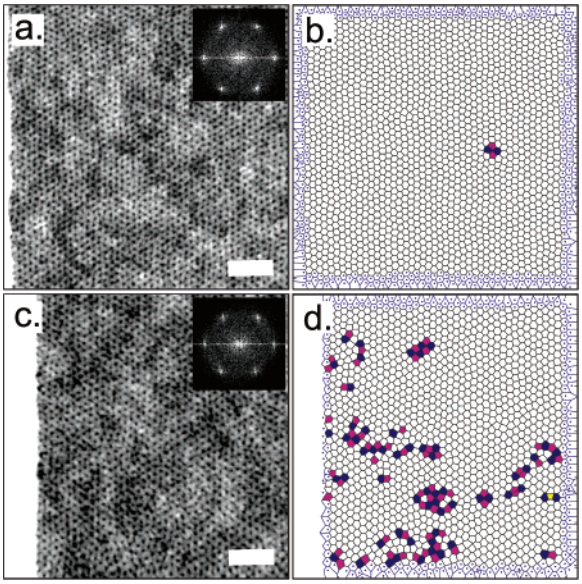

Figure 5. (a, b) $t_f = 41$ nm. The crystal is aligned with the close-packed rows parallel to the edge on the left. The Voronoi analysis shows 1 bound dislocation pair, consisting of two 5-fold and two 7-fold coordinated spheres, colored pink and blue respectively. (c, d) $t_f = 40$ nm. A high density of defects is observed. The lattice still has 6-fold symmetry, and is aligned with the edge of the well. Scale bar = 0.2 μm.

still contains many defects, and these annihilate during the isothermal anneal at a temperature in the crystalline phase.[39] The diffusion barrier is also reduced at higher temperatures,[40] which permits more rapid ordering.

The effect of film thickness is also observed in high-resolution scanning force microscopy measurements of the lattice. In parts a and b of Figure 5, the structure of a 41 nm thick film adjacent to the edge of a well is shown with the corresponding Voronoi diagram. The crystal is aligned with the close-packed rows parallel to the edge, and the Voronoi analysis demonstrates a low defect density (1 bound dislocation pair). The structure of a 40 nm thick film is presented in Figure 5, parts b and c. A high density of defects is observed, although the lattice is on average still aligned with the edge of the well. The effects of an optimal and a suboptimal film thickness are repeatable at any given annealing temperature, but the optimum thickness decreases with increasing temperature. These effects can also be reproduced on a wafer where there is a gradient of thickness in the wells as shown in Appendix 2.

The fact that close-packed rows are always aligned with the edges differs from a previous report where a monolayer of spherical-domain block copolymer was laterally confined in long trenches, and over a range of temperatures encompassing the crystalline to hexatic transition, the close-packed rows of the lattice were oriented $\pm 5°$ with respect to the edge normal.[13] In that case, the topography was produced with an isotropic chemical etch, which is unlikely to produce the near-vertical sidewall angle necessary for graphoepitaxy at high temperatures.

Orientational Order. The diffraction data for films of thickness $t_f = 41$ nm and $t_f = 40$ nm are shown as polar surface plots (to resemble a powder diffraction pattern) in Figure 6, parts a and b. Both data sets demonstrate 6-fold symmetry, but the intensity of the first Bragg peak drops by 95% with the 1 nm decrease in monolayer thickness,[41] signifying a dramatic loss of order. Orientational order is quantified by fitting the $I(\Phi)$ data for the first Bragg reflection to the Fourier series described by eq 4, using the harmonic amplitudes C_{6n} as adjustable parameters. Best fit results from nonlinear regression

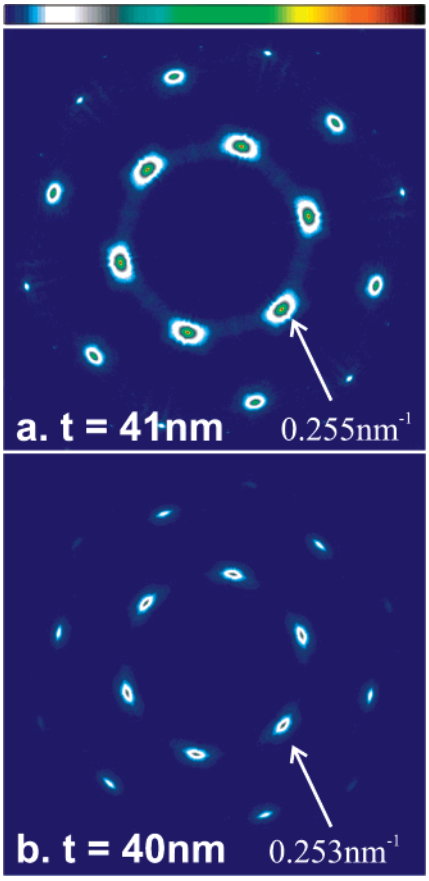

Figure 6. $\ln[I(2\Theta, \alpha_f)]$ diffraction data compiled using the procedure illustrated by Figure 3. (a) Film thickness $t_f = 41$ nm (monolayer plus brush). (b) $t_f = 40$ nm. Both data sets are shown on the same logarithmic scale, with the intensity normalized by the exposure time. The intensity of the first Bragg peak in part b is 5% of that in part a, indicating a loss of order.[41]

are shown in Figure 7, parts a and b. The first three harmonics for a 41 nm thick film are $C_6 = 0.94$, $C_{12} = 0.90$, and $C_{18} = 0.86$, decaying to zero near the 50th harmonic. This indicates that 6-fold orientational order is near perfect, but the higher order harmonics are not fully developed. In contrast, decay in the harmonic amplitudes from a 40 nm thick film is more rapid, with $C_6 = 0.89$, $C_{12} = 0.82$, and $C_{18} = 0.73$, decaying to zero at the 30th harmonic.[42] Fitting the $I(\Phi)$ peaks to a Lorentzian function results in a full width at half-maximum of 1.1° for $t_f = 41$ nm, and 2.4° for $t_f = 40$ nm.

Translational Order. The measured line shape is fit by nonlinear regression to the convolution of the appropriate structure factor with the experimental resolution function, i.e., $I(q) = \int R(k)S(q - k)\,dk$. The peak areas are normalized to unity, and fits are implemented on an Iq^2 scale to accentuate the tails of the peaks. The form factor is excluded from this analysis, because the peak asymmetry due to these oscillations is eliminated by the background correction. Domain size polydispersity will produce a distribution of lattice parameters, but this has little effect on the line shape analysis.[24] The shape of the (10) diffraction peak for both $t_f = 41$ nm and 40 nm cannot be deconvolved from the resolution function. However, KTNHY theory predicts the higher order peaks for the crystalline phase will broaden with the scaling $\eta_G \sim G^2$, and we find that the (11) and (20) reflections for a 41 nm thick film can be successfully fit to the theoretical profiles for a 2D crystal. The behavior measured from a 40 nm thick film is consistent with a hexatic phase, and we find the inverse correlation length κ broadens with increasing G, so we are able to fit the (11), (20),

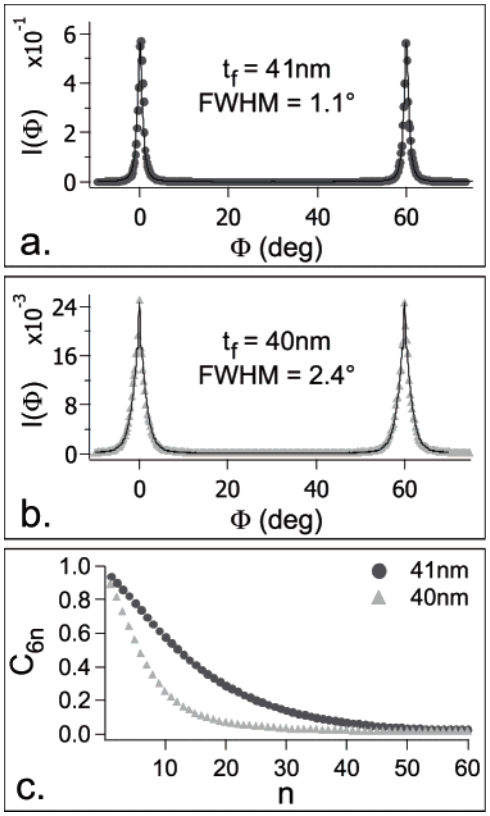

Figure 7. Orientational order as a function of film thickness t_f. (a) $I(\Phi)$ data for a 41 nm thick film fit to the Fourier series described by eq 4, using the harmonic amplitudes C_{6n} as adjustable parameters. Peak areas are normalized to unity. (b) $I(\Phi)$ data for a 40 nm thick film and Fourier series fit. The data scale is relative to that in part a, and we observe a 95% decrease in the peak amplitude. (c) Calculated harmonic amplitudes C_{6n}. The higher order harmonics are the first to decay when the film thickness is decreased.

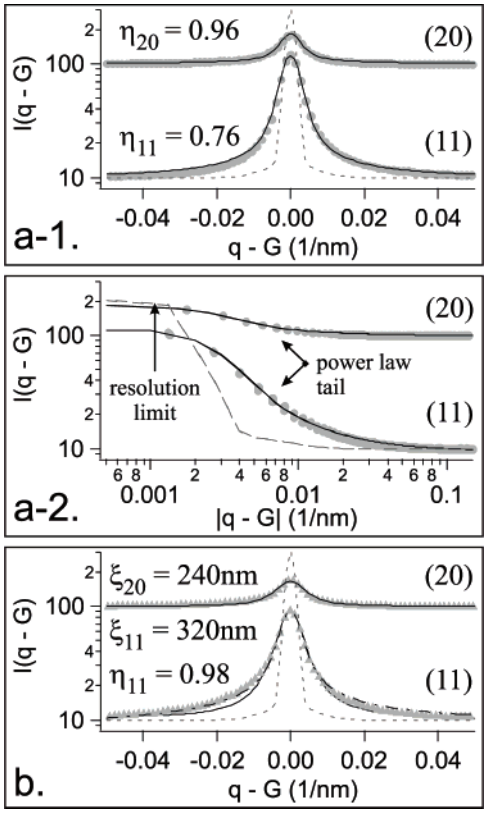

Figure 8. Translational order as a function of film thickness. (a) t_f = 41 nm. $I(q)$ data for the (11) and (20) reflections are fit to the Kummer line shape described by eq 2. Results are shown in log−linear ($a - 1$) and log−log ($a - 2$) plots. (b) t_f = 40 nm. $I(q)$ data for the (11) reflection fit to the Kummer function (dashed-dotted line), and $I(q)$ data for the (11) and (20) peaks fit to Lorentzian line shape (solid lines) described by eq 3. The resolution function (the direct beam profile) is marked by the dashed line. All peak areas are normalized to unity.

and (30) lineshapes. This broadening reflects the sensitivity of the higher order diffraction peaks to defects as well as thermal fluctuations in the lattice.

The (11) and (20) reflections for t_f = 41 nm are simultaneously fit to the crystalline Kummer line shape described by eq 2. Best fit parameters are $\eta_{11} = 0.76$, $\eta_{20} = 0.96$, and $L = 1.5\ \mu$m (approximately the resolution limit) with a mean square error of 0.11.[45,46] Fit results are shown in Figure 8a. From the KTNHY scaling $\eta_G \sim G^2$, the decay exponent associated with the first Bragg reflection is $\eta_{10} = 0.25$. The translational correlation function $g_T(r) \sim r^{-0.25}$ will therefore decay by 45% over 10 lattice parameters, which is unacceptable for patterning applications that require precise domain positioning. We report a decay exponent of $\eta_{10} = 0.2$ at 215 ± 5 °C elsewhere,[24] which suggests that in this case, reduced mobility at 210 °C traps more defects in the lattice. This assertion is supported by SFM results, where heating the monolayer from room-temperature directly to 210 °C results in low-angle grain boundaries in 9 μm wide wells (Figure 4b), but heating directly to 215 °C produces single crystals in wells that are 12 μm wide (Figure 11d).[39]

The (11) and (20) reflections for t_f = 40 nm cannot be simultaneously fit to the Kummer line shape. Fitting the (11) peak independently results in $\eta_{11} = 0.98$ and $L = 1.6\ \mu$m with a mean square error of 0.02. This corresponds with $\eta_{10} = {}^1/_3$ for the first Bragg peak, the theoretical maximum for KTNHY theory, and suggests that the hexatic structure factor is appropriate. Fits to the Lorentzian form described by eq 3 result in the correlation lengths $\xi_{11} = 0.32 \pm 0.01\ \mu$m, $\xi_{20} = 0.24 \pm 0.01\ \mu$m, and $\xi_{30} = 0.047 \pm 0.002\ \mu$m. The scaling for the correlation length ξ as a function of the plane spacing $d = 2\pi/q$ is well fit by an empirical linear relationship, $\xi = 46d - 335$, and we estimate the correlation length associated with the (10) reflection to be 0.8 μm ≈ 28a, where a = 28.7 nm is the lattice parameter. This is consistent with previous reports of the hexatic correlation length (∼11a) measured by scanning force microscopy.[38]

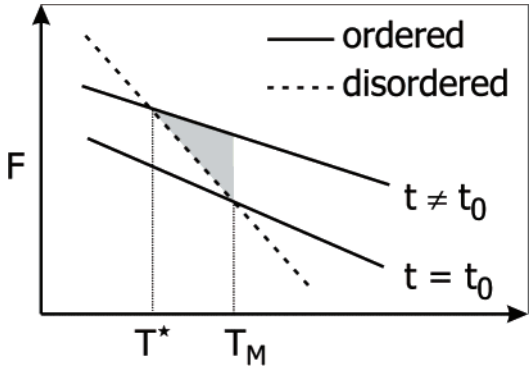

Figure 9. Idealized free energy diagram illustrating the effect of monolayer thickness t on the free energy, and the resulting phase behavior. Assuming the entropy of the disordered state is independent of thickness, the melting temperature T_M could be depressed if the thickness of the crystalline (ordered) phase is not equal to the ideal value t_0. This diagram is drawn for a hypothetical first-order melting transition; However, the same argument holds for the continuous transitions predicted by KTNHY theory. Note $dF/dT = -S$, and entropy contributions dominate the free energy of the disordered state.

Origin of Thickness Dependent Phase Behavior. The dependence of order on monolayer thickness is surprising, since

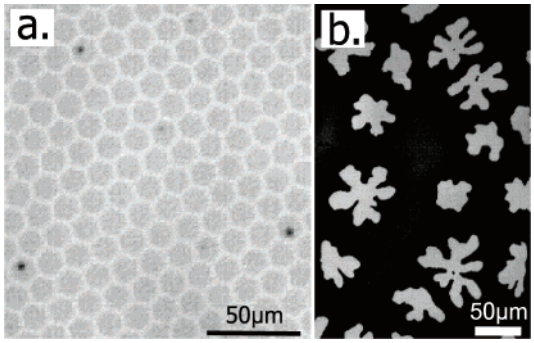

Figure 10. Optical micrographs. (a) A low density of islands is observed on the surface of a 41 nm thick film (dark circular regions in the wells), only at certain radial distances from the center of the wafer (i.e., slight variation in film thickness from spin-casting). Islands are not observed on the surface of a 40 nm thick film. (b) Typical hole structures are observed in a monolayer of spherical-domain PS−PVP on a flat substrate. In this example, the monolayer is approximately 35 nm thick, or 6 nm thinner than optimal. Many of the fingering patterns extend from visible dust particles.

thin films of block copolymers typically form surface relief structures (islands or holes) when the as-cast film thickness is incommensurate with the equilibrium layer periodicity,[47] but there are a few exceptions. Studies of block copolymer lamellae demonstrate conditions where it is more favorable to perturb the layer periodicity than form an island or hole. For example, a barrier to the formation of islands was reported for high molecular weight polymers,[48] and experiments incorporating thickness gradients report a range where deformation of the outer layer is more favorable than forming surface relief structures.[49]

When the film thickness is incommensurate with the natural layer thickness, defects could be generated in an effort to conserve space. For example, it is known that 7-fold and 5-fold coordinated spheres are respectively larger and smaller than 6-fold coordinated sites,[50] so a preponderance of 7-fold defects could stabilize a film that is too thin. Another possibility is the formation of vacancies in the lattice. Absent spheres are not observed in the incompressible block copolymer melt, but pairs of dislocations separated by one row and oriented with the two extra half rows extending out from the pair are similar to vacancies.[19] However, we always observe equal numbers of 5- and 7-fold defect sites, and vacancies in the form of close dislocation pairs are not observed. Therefore, it seems that topological defects do not stabilize the thin monolayer.

A qualitative argument based on entropy contributions to the free energy can be used to describe this thickness dependence. At fixed temperature, the free energy F of an ordered 2D layer is quadratically dependent on the monolayer thickness t with the minimum at an optimal value t_0.[51] Confinement of the 2D crystal to a thickness $t \neq t_0$ results in an entropic penalty: For our experiments, where $t < t_0$, increased stretching of the coronae chains is detected by a shift in the diffraction peak positions to lower q (see Figure 6). In the disordered state, we assume the free energy can be approximated as independent of t. The free energy diagram in Figure 9 demonstrates that if these assumptions are reasonable, the melting temperature is depressed for films of thickness $t \neq t_0$. This reasoning is consistent with a recent study of sheared spherical-domain bilayer films, where the bilayer was confined between two hard boundaries, and a disordered structure was observed when $t \neq t_0$.[9]

In our experiments, the monolayer is not confined in the thickness direction, so disordering would result only if there is an energy barrier to the formation of an island or hole at the free surface. We only observe a barrier to the formation of holes: For example, a very low density of islands is observed on the surface of a 41 nm thick monolayer, shown in Figure 10a. Similar effects have been noted in bilayer films of lamellar block copolymers.[52] In those systems, islands formed for $t > t_0$ shortly after raising the temperature above the glass transition. In contrast, for $t < t_0$, holes were nucleated from impurities in the film, and the morphology developed through a slow nucleation and growth process that resulted in a fractal "fingering" pattern. These different mechanisms were attributed to a much larger free energy barrier to the formation of holes, which is predicted by mean field theory. We observe similar fractal hole patterns in monolayers thinner than optimal prepared on flat substrates. An example of this morphology is shown in Figure 10b, where the initial film thickness was approximately $t_f \approx 35$ nm. We have not been able to prepare "thin" monolayers on flat substrates: There are always a few particles on the surface that can nucleate holes, which then grow as large as several millimeters in diameter. In contrast, lateral confinement of the monolayer in 12 μm wide hexagonal wells prevents the growth of macroscopic hole structures.

The Shear Modulus of a 2D Crystal. Diffraction from 2D block copolymer crystals also measures the shear modulus of the monolayer.[24,53] Referring back to eq 1, the KTNHY decay exponent η_G is a function of the independent Lamé constants μ and λ, which characterize the elasticity of a 2D hexagonal lattice.[54] The bulk modulus is $B = \lambda + \mu$, and the shear modulus is μ. Thermodynamic stability requires both the shear modulus and bulk modulus to be positive, and $\lambda > 0$ for an ordered block copolymer like PS−PVP whose elasticity can be described roughly by pairwise micelle−micelle interactions (having a positive Poisson's ratio), resulting in the bounds $1 < c(\mu, \lambda) < 1.5$. This provides an estimate for μ within a factor of 1.5, and we find $\mu = 1.42c \times 10^{-4}$ N/m. This approximation can be further refined using predictions for λ/μ from self-consistent mean field theory, which is described in Appendix 1. These simulations, conducted at $\chi N = 60$ and $f = 0.12$, produced a value $\lambda/\mu = 1.1$. Therefore, $c = 1.32$ and $\mu = 1.9 \times 10^{-4}$ N/m.

Theoretical approaches to estimate the 2D elastic constants could direct the design of block copolymer systems for patterning applications. The shear modulus is the physical parameter that has the strongest influence on translational order, so selecting systems with a high shear modulus will result in better domain positioning (as $\mu \to \infty$, $\eta_G \to 0$, $g_T(r) \to$ constant). In bulk systems, the shear modulus is strongly dependent on the lattice spacing, scaling with the form $\mu_0 \sim d^{-3}$.[55,56] Therefore, at a fixed value of χN, better ordering will be observed when N is small, and χ is large.

Conclusions

We demonstrate an effect of film thickness on 2D ordering of spherical-domain block copolymers, characterized by grazing-incidence small-angle X-ray diffraction. The monolayer of hexagonally packed spheres, which has a periodicity of 29 nm, is laterally confined in hexagonal wells that are 12 μm wide and 26 nm deep. When the total film thickness (monolayer plus brush) is 41 nm at 210 °C, slow cooling from the order−disorder transition produces oriented single crystals in each well, with algebraically decaying translational order of the form $g_T(r) \sim r^{-0.25}$, and long-range 6-fold orientational order with a full width at half-maximum of 1.1°. Decreasing the film thickness to 40 nm at 210 °C results in hexatic ordering, where the translational correlation length is on the order of 0.5 μm, orientational order is diminished (particularly the higher order harmonics), and the full width at half-maximum is 2.4°. Direct measurement of the

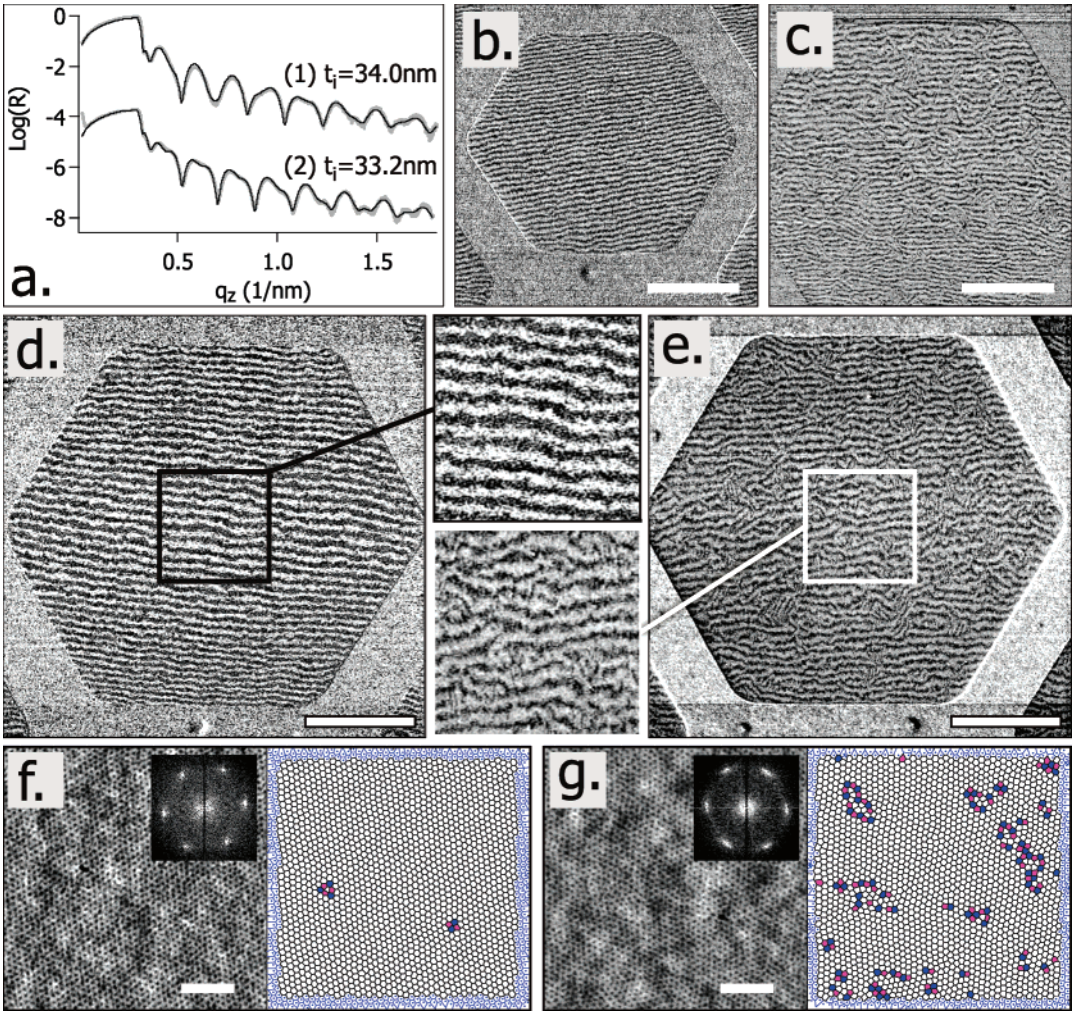

Figure 11. (a) X-ray reflectivity of initial film thicknesses t_i (measured from the control areas of the substrates). The Kiessig fringes result from interference between the polymer and oxide layers. (b, c) A thickness "gradient" is produced by varying the width of the hexagonal well while keeping the width of the mesa constant. The hexagonal well in part b is 9 μm wide, and the thickness of the film in the well is $t_f \approx 40$ nm. The structure is characterized by moiré interference patterns, demonstrating a well-ordered single grain. The hexagonal well in part c is 12 μm wide, and $t_f \approx 39$ nm. The disorder in the moiré fringes corresponds with underlying dislocation defects in the block copolymer lattice. The two regions of the sample shown in parts b and c are separated by less than 100 μm. (d−g) The hexagonal wells are 12 μm wide. (d) Moiré patterns, $t_f \approx 40$ nm. (e) Moiré patterns, $t_f \approx 39$ nm. (f) Direct measurement of the lattice, $t_f \approx 40$ nm. The Voronoi analysis demonstrates a low density of bound dislocation pairs. (g) Direct measurement of the lattice, $t_f \approx 39$ nm. The Voronoi analysis demonstrates a high density of 5 and 7-fold sites, colored pink and blue respectively. The scale bar is 3.5 μm in b−e and 0.25 μm in f and g.

lattice with both high resolution and moiré interference scanning force microscopy provides qualitative support for the diffraction data. We propose a simple free energy model to explain the stability of the hexatic over the crystalline phase when the film thickness is incommensurate with the natural layer thickness.

Acknowledgment. We appreciate financial support from NSF DMR Polymers Program Award No. DMR-07-04539. Use of the APS was supported by the U.S. DOE, Office of Science, Office of Basic Energy Sciences, under Contract No. DE-AC02-06CH11357. This work benefitted from use of the facilities of the UCSB MRL, which is supported by the MRSEC Program of the NSF under Award No. DMR05-20415, and from use of the nanofabrication facilities, which is supported by the NSF−NNIN under Award No. 44771-7475. We thank R. A. Segalman for synthesis of the PS−PVP diblock copolymer utilized in these studies, B. Thibeault for assistance with lithography, the Sector 8 staff for beamline support, and C.R. Safinya for many helpful discussions.

Appendix 1

Calculation of the Elastic Constants for a 2D Hexagonal Crystal of Spherical Block Copolymer. A 2D hexagonal crystal has two independent elastic moduli. The change of dimensionless free energy density for a small two-dimensional strain of a monolayer of hexagonally packed spheres can be written as[57]

$$\frac{N\delta F}{\rho_0 V k_B T} = \frac{1}{2}\frac{V_c B}{tRT}(\epsilon_{11}+\epsilon_{22})^2 + \frac{V_c \mu}{tRT}\left(\left(\epsilon_{11} - \frac{1}{2}tr\,\underline{\underline{\epsilon}}\right)^2 + \left(\epsilon_{22} - \frac{1}{2}tr\,\underline{\underline{\epsilon}}\right)^2 + \epsilon_{12}^2 + \epsilon_{21}^2\right) \quad (5)$$

where B and μ represent the bulk and shear modulus, respectively. In eq 5, N is the polymerization index, ρ_0 is the segment number density, k_BT is thermal energy, $\underline{\underline{\epsilon}}$ is the strain tensor, V_c is the molar volume of a polymer, and t is the optimized thickness of the monolayer. The bulk modulus, B, can also be related to the Lamé constant λ through the relation $B = \lambda + \mu$

since $\delta F/A = (1/2)\lambda\epsilon_{ii}^2 + \mu\epsilon_{ik}^2$, where A is the area of the monolayer.

The Lamé constants for a 2D hexagonal crystal are calculated using numerical self-consistent field theory in a parallelepiped coordinate cell where the strain tensor, $\underline{\underline{\epsilon}}$, is related to a cell shape tensor, $\underline{\underline{h}}$[58,59]

$$\underline{\underline{\epsilon}} = \frac{1}{2}((\underline{\underline{h}}_0^T)^{-1}\underline{\underline{h}}^T\underline{\underline{h}}(\underline{\underline{h}}_0)^{-1} - \underline{\underline{1}}) \tag{6}$$

and where $\underline{\underline{1}}$ denotes the unit tensor. The subscript, 0, represents the stress-free state. The 2D cell shape tensor can be expressed as

$$\underline{\underline{h}} = \begin{pmatrix} L_1 & L_2 \cos\alpha \\ 0 & L_2 \sin\alpha \end{pmatrix} \tag{7}$$

where L_i is the length of the ith side of the simulation cell and α is the angle between adjacent sides. For the stress-free state corresponding to a unit cell of the hexagonal lattice with parameters $\chi N = 60$ and $f = 0.12$, we find $L_1 = L_2 = 3.81228\ R_{g0}$, $t = 3.48388\ R_{g0}$, and $\alpha = 120°$, where R_{g0} is the ideal radius of gyration of the block copolymer.

The Lamé constants are calculated from the following procedure:

1. Isotropic dilation ($\epsilon_{11} = \epsilon_{22} \sim 0.01, 0.02, 0.025$) produces only diagonal strain components, which can be used to determine the bulk modulus, B.

2. Shear deformation at constant volume provides access to the shear modulus, μ. For this purpose, we hold $\epsilon_{11} = \epsilon_{22} = 0$ and vary $\epsilon_{12} = \epsilon_{21} \sim 0.005, 0.01, 0.015, 0.025$.

3. λ is calculated from the numerical estimates for B and μ.

Throughout the above procedure, the free energy is minimized at each strain step with regard to the thickness t of the monolayer film (orthogonal to the 2D parallelepiped cell). Periodic boundary conditions are applied at the two film surfaces. In the simulations, 64^3 collocation points and 600 contour steps are used in order to reduce the error of the dimensionless free energy density below order $\sim 10^{-7}$.

Our simulations conducted at $\chi N = 60$ and $f = 0.12$ led to the following values for the elastic constants: $V_c B/tRT = 0.68303$, $V_c\mu/tRT = 0.32420$, and $V_c\lambda/tRT = 0.35883$. From these results, $\lambda/\mu = 1.10683$ and $c = 1.32187$ are obtained.

Appendix 2

Thickness Gradients. In this section, a method to produce a thickness gradient using lithographically patterned substrates is outlined. The data from such samples demonstrate that the disordering effect reported in this paper is a consequence of incommensurability between the as-cast film thickness and the equilibrium layer thickness, and not the result of poor temperature control or chance thermal fluctuations.

The lithography methods are the same as described in the experimental section of this paper, but a different photomask is used to produce the hexagonal features, and only *half* of the 2 in. diameter substrate is patterned. The features are arrays of hexagonal wells, where the width of the mesas is fixed at 2 μm, and the width of the wells varies from 2 to 100 μm between parallel sides. Each array spans an area of $\sim 0.1-0.2$ mm^2. A PS−PVP film covering the entire substrate with a uniform film thickness t_i is produced by spin-casting. The wafer is then cracked in half to separate the patterned area from the unpatterned control region. The patterned area is divided into ~ 0.5 cm^2 pieces that are annealed individually at different temperatures/times. The control region is used to determine the thickness t_i.

The control samples were annealed under high vacuum at 110 °C for several hours to remove the residual solvent. The as-cast film thicknesses t_i and the thickness of the oxide layers were measured by X-ray reflectivity as previously described. Results are shown in Figure 11a, with $t_i = 34 \pm 0.1$ nm/$\chi^2 = 19$ for profile 1 and $t_i = 33.2 \pm 0.1$ nm/$\chi^2 = 9$ for profile 2.

The patterned samples were heated from room temperature to 215 ± 5 °C and annealed isothermally for 3−4 days. This is the lowest temperature where direct annealing results in a single-crystal spanning 12 μm wide hexagonal wells,[39] and is well above the glass transition for PS−PVP (100 °C), so excess material from the mesas is drawn into the wells during the early stages of annealing. The resulting thickness of the film in the well is

$$t_f = a + b = \frac{t_i(A_W + A_M) - bA_M}{A_W} \tag{8}$$

where "a" and "b" are the monolayer and brush thicknesses, A_W is the area of the well, and A_M is the area of the mesa. The dependence of film thickness on the area of the well results in the thickness "gradient". At 215 °C, the brush thickness is estimated to be 18 ± 1 nm.[39] Due to uncertainty in the brush thickness, t_f values reported here are approximate.

Results for the "gradient" are shown in Figure 11b,c (t_i = 33.2 nm). A 40 nm thick film produced by confinement in 9 μm wide wells is extremely well-ordered, as evidenced by the highly regular moiré interference patterns. A 39 nm thick film, which results from confinement in the 12 μm wide wells, contains a high density of dislocation defects. These two regions on the substrate are separated by less than 100 μm. Parts d−g of Figure 11 show the structure for 40 nm ($t_i = 34$) and 39 nm ($t_i = 33.2$) thick films laterally confined in 12 μm wide wells. These result from two different samples, but clearly demonstrate that the disordered structure in Figure 11c is not kinetically trapped but is an effect of film thickness.

References and Notes

(1) Bates, F. S.; Fredrickson, G. H. *Annu. Rev. Phys. Chem.* **1990**, *41*, 525−557.
(2) Naito, K.; Hieda, H.; Sakurai, M.; Kamata, Y.; Asakawa, K. *IEEE Trans. Magn.* **2002**, *38*, 1949−1951 Part 1.
(3) Morkved, T. L.; Lu, M.; Urbas, A. M.; Ehrichs, E. E.; Jaeger, H. M.; Mansky, P.; Russell, T. P. *Science* **1996**, *273*, 931−933.
(4) Wang, J. Y.; Xu, T.; Leiston-Belanger, J. M.; Gupta, S.; Russell, T. P. *Phys. Rev. Lett.* **2006**, *96*, 128301−128304.
(5) Kim, S. O.; Solak, H. H.; Stoykovich, M. P.; Ferrier, N. J.; de Pablo, J. J.; Nealey, P. F. *Nature (London)* **2003**, *424*, 411−414.
(6) Stoykovich, M. P.; Muller, M.; Kim, S. O.; Solak, H. H.; Edwards, E. W.; de Pablo, J. J.; Nealey, P. F. *Science* **2005**, *308*, 1442−1446.
(7) Wilmes, G. M.; Durkee, D. A.; Balsara, N. P.; Liddle, J. A. *Macromolecules* **2006**, *39*, 2435−2437.
(8) Angelescu, D. E.; Waller, J. H.; Adamson, D. H.; Deshpande, P.; Chou, S. Y.; Register, R. A.; Chaikin, P. M. *Adv. Mater.* **2004**, *16*, 1736−1739.
(9) Angelescu, D. E.; Waller, J. H.; Register, R. A.; Chaikin, P. M. *Adv. Mater.* **2005**, *17*, 1878−1881.
(10) Segalman, R. A.; Yokoyama, H.; Kramer, E. J. *Adv. Mater.* **2001**, *13*, 1152−1156.
(11) Cheng, J. Y.; Ross, C. A.; Thomas, E. L.; Smith, H. I.; Vancso, G. J. *Appl. Phys. Lett.* **2002**, *81*, 3657−3659.
(12) Sundrani, D.; Darling, S. B.; Sibener, S. J. *Langmuir* **2004**, *20*, 5091−5099.
(13) Segalman, R. A.; Hexemer, A.; Kramer, E. J. *Macromolecules* **2003**, *36*, 6831−6839.
(14) Cheng, J. Y.; Ross, C. A.; Thomas, E. L.; Smith, H. I.; Vancso, G. J. *Adv. Mater.* **2003**, *15*, 1599−1602.

(15) Cheng, J. Y.; Mayes, A. M.; Ross, C. A. *Nat. Mater.* **2004**, *3*, 823−828.
(16) Cheng, J. Y.; Zhang, F.; Smith, H. I.; Vancso, G. J.; Ross, C. A. *Adv. Mater.* **2006**, *18*, 597−600.
(17) Mermin, N. D. *Phys. Rev.* **1968**, *176*, 250−254.
(18) Halperin, B. I.; Nelson, D. R. *Phys. Rev. Lett.* **1978**, *41*, 121−124.
(19) Nelson, D. R.; Halperin, B. I. *Phys. Rev. B* **1979**, *19*, 2457−2484.
(20) Kosterlitz, J. M.; Thouless, D. J. *J. Phys. C, Solid State Phys.* **1973**, *6*, 1181−1203.
(21) Young, A. P. *Phys. Rev. B* **1979**, *19*, 1855−1866.
(22) Segalman, R. A.; Hexemer, A.; Hayward, R. C.; Kramer, E. J. *Macromolecules* **2003**, *36*, 3272−3288.
(23) Angelescu, D. E.; Harrison, C. K.; Trawick, M. L.; Register, R. A.; Chaikin, P. M. *Phys. Rev. Lett.* **2005**, *95*.
(24) Stein, G. E.; Kramer, E. J.; Li, X.; Wang, J. *Phys. Rev. Lett.* **2007**, *98*, 086101.
(25) Dutta, P.; Sinha, S. K. *Phys. Rev. Lett.* **1981**, *47*, 50−53.
(26) Wolfram, S. *The Mathematica Book*, 3rd ed.; Wolfram Media/Cambridge University Press: Cambridge, U.K., 1996.
(27) Aeppli, G.; Bruinsma, R. *Phys. Rev. Lett.* **1984**, *53*, 2133−2136.
(28) Brock, J. D.; Birgeneau, R. J.; Litster, J. D.; Aharony, A. *Phys. Today* **1989**, *42*, 52−59.
(29) Segalman, R. A.; Schaefer, K. E.; Fredrickson, G. H.; Kramer, E. J.; Magonov, S. *Macromolecules* **2003**, *36*, 4498−4506.
(30) The large radius of curvature in the corners of the hexagonal wells produces localized defects: Approximately 10−20 rows of spheres wrap around the corner, then the orientation reverts to that induced by the straight walls. The "defective" regions of the wells constitute approximately 2% of the total well area, and as such, the contribution to the total diffracted intensity is negligible.
(31) Parratt, L. G. *Phys. Rev.* **1954**, *95*, 359−369.
(32) Tolan, M. *X-Ray Scattering from Soft-Matter Thin Films*; Springer Tracts in Modern Physics 148; Springer-Verlag: Berlin, 1999.
(33) Gibaud, A.; Vignaud, G.; Sinha, S. K. *Acta Crystallogr.* **1993**, *A49*, 642−648.
(34) Tolan, M.; Bahr, D.; Sussenbach, J.; Press, W.; Brinkop, F.; Kotthaus, J. P. *Physica B* **1994**, *198*, 55−57.
(35) Salditt, T.; Rhan, H.; Metzger, T. H.; Peisl, J.; Schuster, R.; Kotthaus, J. P. *Z. Phys. B-Condens. Matter* **1994**, *96*, 227−230.
(36) Angelescu, D. E.; Harrison, C. K.; Trawick, M. L.; Chaikin, P. M.; Register, R. A.; Adamson, D. H. *Appl. Phys. a: Mater. Sci. Process.* **2004**, *78*, 387−392.
(37) Hexemer, A.; Stein, G. E.; Kramer, E. J.; Magonov, S. *Macromolecules* **2005**, *38*, 7083−7089.
(38) Segalman, R. A.; Hexemer, A.; Kramer, E. J. *Phys. Rev. Lett.* **2003**, *91*, 196101.
(39) Stein, G. E. Ordering of spherical domain block copolymers in monolayers and multilayers. Thesis, University of California, Santa Barbara, CA, 2006.
(40) Yokoyama, H.; Kramer, E. J.; Rafailovich, M. H.; Sokolov, J.; Schwarz, S. A. *Macromolecules* **1998**, *31*, 8826−8830.
(41) The normalization is not exact. Scattering from the microstructure is amplified by coherent interference between the reflected and transmitted waves inside the film, and this amplification is highly sensitive to the incident angle, which is difficult to calibrate.[60] The scattering volume is proportional to the beam footprint, which is also sensitive to incident angle (see Figure 2d). By comparing different samples having the same film thickness (within experimental error), we find that the intensity of the (10) peak is reduced by 60−95%.
(42) Note that $C_{6n} \equiv \mathrm{Re}\langle\Psi^n\rangle$, where $\Psi(r) = \exp(i6\theta(r))$, and $\theta(r)$ is the angle between the close-packed rows of the hexagonal lattice and a reference axis. The harmonic amplitudes are found to decay with the empirical scaling $C_{6n} \sim C_6^{\sigma_n}$, where $\sigma_n = n$. At the transition to hexatic order, this is the scaling predicted by mean field theory.[43] However, corrections for fluctuations in the phase of Ψ lead to $\sigma_n = n^2$ in 2D.[44] We are unable to fit the data for 40 nm thick films to this form. It is possible that 2D confinement stabilizes the orientation during this "melting" transition, leading to a larger orientational order parameter.
(43) Aharony, A.; Birgeneau, R. J.; Brock, J. D.; Litster, J. D. *Phys. Rev. Lett.* **1986**, *57*, 1012−1015.
(44) Paczuski, M.; Kardar, M. *Phys. Rev. Lett.* **1988**, *60*, 861.
(45) If the (11) and (20) reflections are fit individually, we find $L = 1.7$ μm and $\eta_{11} = 0.77$ for the (11) peak, and $L = 1.3$ μm and $\eta_{20} = 0.87$ for the (20) reflection. From the KTNHY scaling, the decay exponent associated with the (10) reflection is $\eta_{10} = 0.24 \pm 0.02$, consistent with the result from simultaneous fits. The simultaneous fit is helpful because the parameters L and η_G are coupled.
(46) The resolution limit L_R is estimated by fitting the beam profile to the Kummer lineshape (equation 2) with $\eta_{10} = 0$, which has the Gaussian form $\sim \exp\{-q^2L^2/4\pi\}$. This results in the limit $L_R = 2$ μm, an overestimate since the beam is broader than a single Gaussian peak.
(47) Fasolka, M. J.; Mayes, A. M. *Annu. Rev. Mater. Res.* **2001**, *31*, 323−355.
(48) Russell, T. P.; Menelle, A.; Anastasiadis, S. H.; Satija, S. K.; Majkrzak, C. F. *Macromolecules* **1991**, *24*, 6263−6269.
(49) Smith, A. P.; Douglas, J. F.; Meredith, J. C.; Amis, E. J.; Karim, A. *J. Polym. Sci., Part B: Polym. Phys.* **2001**, *39*, 2141−2158.
(50) Hammond, M. R.; Sides, S. W.; Fredrickson, G. H.; Kramer, E. J.; Ruokolainen, J.; Hahn, S. F. *Macromolecules* **2003**, *36*, 8712−8716.
(51) Matsen, M. W. *J. Chem. Phys.* **1997**, *106*, 7781−7791.
(52) Koneripalli, N.; Bates, F. S.; Fredrickson, G. H. *Phys. Rev. Lett.* **1998**, *81*, 1861−1864.
(53) Safinya, C.; Shen, Y. *Physics of Biomaterials: Fluctuations, Self assembly, and Evolution*; NATO ASI Series E: Applied Sciences 322; Kluwer Academic Publishers: Kluwer, Dordrecht, The Netherlands, 1995.
(54) Chaikin, P. M.; Lubensky, T. C. *Principles of condensed matter physics*; Cambridge University Press: Cambridge, U.K., 1995.
(55) Kossuth, M. B.; Morse, D. C.; Bates, F. S. *J. Rheol.* **1999**, *43*, 167−196.
(56) Sebastian, J. M.; Graessley, W. W.; Register, R. A. *J. Rheol.* **2002**, *46*, 863−879.
(57) Landau, L.; Lifshitz, E. *Theory of Elasticity*, 3rd ed; Pergamon: New York, 1980.
(58) Fredrickson, G. *The Equilibrium Theory of Inhomogeneous Polymers*; Oxford University Press: Oxford, U.K., 2006.
(59) Barrat, J.; Fredrickson, G.; Sides, S. *J. Phys. Chem. B* **2005**, *109*, 6694−6700.
(60) Stein, G. E.; Kramer, E. J.; Li, X.; Wang, J. *Macromolecules* **2007**, *40*, 2453−2460.

MA062559A